

Measurement of the differential cross section for the production of an isolated photon with associated jet in $p\bar{p}$ collisions at $\sqrt{s}=1.96$ TeV

V.M. Abazov³⁶, B. Abbott⁷⁵, M. Abolins⁶⁵, B.S. Acharya²⁹, M. Adams⁵¹, T. Adams⁴⁹, E. Aguilo⁶, S.H. Ahn³¹, M. Ahsan⁵⁹, G.D. Alexeev³⁶, G. Alkhazov⁴⁰, A. Alton^{64,a}, G. Alverson⁶³, G.A. Alves², M. Anastasoae³⁵, L.S. Ancu³⁵, T. Andeen⁵³, S. Anderson⁴⁵, B. Andrieu¹⁷, M.S. Anzels⁵³, M. Aoki⁵⁰, Y. Arnoud¹⁴, M. Arov⁶⁰, M. Arthaud¹⁸, A. Askew⁴⁹, B. Åsman⁴¹, A.C.S. Assis Jesus³, O. Atramentov⁴⁹, C. Avila⁸, F. Badaud¹³, A. Baden⁶¹, L. Bagby⁵⁰, B. Baldin⁵⁰, D.V. Bandurin⁵⁹, P. Banerjee²⁹, S. Banerjee²⁹, E. Barberis⁶³, A.-F. Barfuss¹⁵, P. Bargassa⁸⁰, P. Baringer⁵⁸, J. Barreto², J.F. Bartlett⁵⁰, U. Bassler¹⁸, D. Bauer⁴³, S. Beale⁶, A. Bean⁵⁸, M. Begalli³, M. Begel⁷³, C. Belanger-Champagne⁴¹, L. Bellantoni⁵⁰, A. Bellavance⁵⁰, J.A. Benitez⁶⁵, S.B. Beri²⁷, G. Bernardi¹⁷, R. Bernhard²³, I. Bertram⁴², M. Besançon¹⁸, R. Beuselinck⁴³, V.A. Bezzubov³⁹, P.C. Bhat⁵⁰, V. Bhatnagar²⁷, C. Biscarat²⁰, G. Blazey⁵², F. Blekman⁴³, S. Blessing⁴⁹, D. Bloch¹⁹, K. Bloom⁶⁷, A. Boehnlein⁵⁰, D. Boline⁶², T.A. Bolton⁵⁹, E.E. Boos³⁸, G. Borissov⁴², T. Bose⁷⁷, A. Brandt⁷⁸, R. Brock⁶⁵, G. Brooijmans⁷⁰, A. Bross⁵⁰, D. Brown⁸¹, N.J. Buchanan⁴⁹, D. Buchholz⁵³, M. Buehler⁸¹, V. Buescher²², V. Bunichev³⁸, S. Burdin^{42,b}, S. Burke⁴⁵, T.H. Burnett⁸², C.P. Buszello⁴³, J.M. Butler⁶², P. Calfayan²⁵, S. Calvet¹⁶, J. Cammin⁷¹, W. Carvalho³, B.C.K. Casey⁵⁰, H. Castilla-Valdez³³, S. Chakrabarti¹⁸, D. Chakraborty⁵², K. Chan⁶, K.M. Chan⁵⁵, A. Chandra⁴⁸, F. Charles^{19,‡}, E. Cheu⁴⁵, F. Chevallier¹⁴, D.K. Cho⁶², S. Choi³², B. Choudhary²⁸, L. Christofek⁷⁷, T. Christoudias⁴³, S. Cihangir⁵⁰, D. Claes⁶⁷, J. Clutter⁵⁸, M. Cooke⁸⁰, W.E. Cooper⁵⁰, M. Corcoran⁸⁰, F. Couderc¹⁸, M.-C. Cousinou¹⁵, S. Crépe-Renaudin¹⁴, D. Cutts⁷⁷, M. Cwiok³⁰, H. da Motta², A. Das⁴⁵, G. Davies⁴³, K. De⁷⁸, S.J. de Jong³⁵, E. De La Cruz-Burelo⁶⁴, C. De Oliveira Martins³, J.D. Degenhardt⁶⁴, F. Déliot¹⁸, M. Demarteau⁵⁰, R. Demina⁷¹, D. Denisov⁵⁰, S.P. Denisov³⁹, S. Desai⁵⁰, H.T. Diehl⁵⁰, M. Diesburg⁵⁰, A. Dominguez⁶⁷, H. Dong⁷², L.V. Dudko³⁸, L. Duflo¹⁶, S.R. Dugad²⁹, D. Duggan⁴⁹, A. Duperrin¹⁵, J. Dyer⁶⁵, A. Dyshkant⁵², M. Eads⁶⁷, D. Edmunds⁶⁵, J. Ellison⁴⁸, V.D. Elvira⁵⁰, Y. Enari⁷⁷, S. Eno⁶¹, P. Ermolov³⁸, H. Evans⁵⁴, A. Evdokimov⁷³, V.N. Evdokimov³⁹, A.V. Ferapontov⁵⁹, T. Ferbel⁷¹, F. Fiedler²⁴, F. Filthaut³⁵, W. Fisher⁵⁰, H.E. Fisk⁵⁰, M. Fortner⁵², H. Fox⁴², S. Fu⁵⁰, S. Fuess⁵⁰, T. Gadfort⁷⁰, C.F. Galea³⁵, E. Gallas⁵⁰, C. Garcia⁷¹, A. Garcia-Bellido⁸², V. Gavrilov³⁷, P. Gay¹³, W. Geist¹⁹, D. Gelé¹⁹, C.E. Gerber⁵¹, Y. Gershtein⁴⁹, D. Gillberg⁶, G. Ginther⁷¹, N. Gollub⁴¹, G.A. Golovanov³⁶, B. Gómez⁸, A. Goussiou⁸², P.D. Grannis⁷², H. Greenlee⁵⁰, Z.D. Greenwood⁶⁰, E.M. Gregores⁴, G. Grenier²⁰, Ph. Gris¹³, J.-F. Grivaz¹⁶, A. Grohsjean²⁵, S. Grünendahl⁵⁰, M.W. Grünewald³⁰, F. Guo⁷², J. Guo⁷², G. Gutierrez⁵⁰, P. Gutierrez⁷⁵, A. Haas⁷⁰, N.J. Hadley⁶¹, P. Haefner²⁵, S. Hagopian⁴⁹, J. Haley⁶⁸, I. Hall⁶⁵, R.E. Hall⁴⁷, L. Han⁷, K. Harder⁴⁴, A. Harel⁷¹, J.M. Hauptman⁵⁷, R. Hauser⁶⁵, J. Hays⁴³, T. Hebbeker²¹, D. Hedin⁵², J.G. Hegeman³⁴, A.P. Heinson⁴⁸, U. Heintz⁶², C. Hensel^{22,d}, K. Herner⁷², G. Hesketh⁶³, M.D. Hildreth⁵⁵, R. Hirosky⁸¹, J.D. Hobbs⁷², B. Hoeneisen¹², H. Hoeth²⁶, M. Hohlfeld²², S.J. Hong³¹, S. Hossain⁷⁵, P. Houben³⁴, Y. Hu⁷², Z. Hubacek¹⁰, V. Hynek⁹, I. Iashvili⁶⁹, R. Illingworth⁵⁰, A.S. Ito⁵⁰, S. Jabeen⁶², M. Jaffré¹⁶, S. Jain⁷⁵, K. Jakobs²³, C. Jarvis⁶¹, R. Jesik⁴³, K. Johns⁴⁵, C. Johnson⁷⁰, M. Johnson⁵⁰, A. Jonckheere⁵⁰, P. Jonsson⁴³, A. Juste⁵⁰, E. Kajfasz¹⁵, J.M. Kalk⁶⁰, D. Karmanov³⁸, P.A. Kasper⁵⁰, I. Katsanos⁷⁰, D. Kau⁴⁹, V. Kaushik⁷⁸, R. Kehoe⁷⁹, S. Kermiche¹⁵, N. Khalatyan⁵⁰, A. Khanov⁷⁶, A. Kharchilava⁶⁹, Y.M. Kharzhev³⁶, D. Khatidze⁷⁰, T.J. Kim³¹, M.H. Kirby⁵³, M. Kirsch²¹, B. Klima⁵⁰, J.M. Kohli²⁷, J.-P. Konrath²³, D.E. Korablev³⁶, A.V. Kozelov³⁹, J. Kraus⁶⁵, D. Krop⁵⁴, T. Kuhl²⁴, A. Kumar⁶⁹, A. Kupco¹¹, T. Kurča²⁰, V.A. Kuzmin³⁸, J. Kvita⁹, F. Lacroix¹³, D. Lam⁵⁵, S. Lammers⁷⁰, G. Landsberg⁷⁷, P. Lebrun²⁰, W.M. Lee⁵⁰, A. Leflat³⁸, J. Lellouch¹⁷, J. Leveque⁴⁵, J. Li⁷⁸, L. Li⁴⁸, Q.Z. Li⁵⁰, S.M. Lietti⁵, J.G.R. Lima⁵², D. Lincoln⁵⁰, J. Linnemann⁶⁵, V.V. Lipaev³⁹, R. Lipton⁵⁰, Y. Liu⁷, Z. Liu⁶, A. Lobodenko⁴⁰, M. Lokajicek¹¹, P. Love⁴², H.J. Lubatti⁸², R. Luna³, A.L. Lyon⁵⁰, A.K.A. Maciel², D. Mackin⁸⁰, R.J. Madaras⁴⁶, P. Mättig²⁶, C. Magass²¹, A. Magerkurth⁶⁴, P.K. Mal⁸², H.B. Malbouisson³, S. Malik⁶⁷, V.L. Malyshev³⁶, H.S. Mao⁵⁰, Y. Maravin⁵⁹, B. Martin¹⁴, R. McCarthy⁷², A. Melnitchouk⁶⁶, L. Mendoza⁸, P.G. Mercadante⁵, M. Merkin³⁸, K.W. Merritt⁵⁰, A. Meyer²¹, J. Meyer^{22,d}, T. Millet²⁰, J. Mitrevski⁷⁰, R.K. Mommsen⁴⁴, N.K. Mondal²⁹, R.W. Moore⁶, T. Moulik⁵⁸, G.S. Muanza²⁰, M. Mulhearn⁷⁰, O. Mundal²², L. Mundim³, E. Nagy¹⁵, M. Naimuddin⁵⁰, M. Narain⁷⁷, N.A. Naumann³⁵, H.A. Neal⁶⁴, J.P. Negret⁸, P. Neustroev⁴⁰, H. Nilsen²³, H. Nogima³, S.F. Novaes⁵, T. Nunnemann²⁵, V. O'Dell⁵⁰, D.C. O'Neil⁶, G. Obrant⁴⁰, C. Ochando¹⁶, D. Onoprienko⁵⁹, N. Oshima⁵⁰, N. Osman⁴³, J. Osta⁵⁵, R. Otec¹⁰, G.J. Otero y Garzón⁵⁰, M. Owen⁴⁴, P. Padley⁸⁰, M. Pangilinan⁷⁷, N. Parashar⁵⁶, S.-J. Park^{22,d}, S.K. Park³¹, J. Parsons⁷⁰, R. Partridge⁷⁷, N. Parua⁵⁴, A. Patwa⁷³, G. Pawloski⁸⁰, B. Penning²³, M. Perfilov³⁸, K. Peters⁴⁴, Y. Peters²⁶, P. Pétroff¹⁶, M. Petteni⁴³, R. Piegaia¹,

J. Piper⁶⁵, M.-A. Pleier²², P.L.M. Podesta-Lerma^{33,c}, V.M. Podstavkov⁵⁰, Y. Pogorelov⁵⁵, M.-E. Pol², P. Polozov³⁷, B.G. Pope⁶⁵, A.V. Popov³⁹, C. Potter⁶, W.L. Prado da Silva³, H.B. Prosper⁴⁹, S. Protopopescu⁷³, J. Qian⁶⁴, A. Quadt^{22,d}, B. Quinn⁶⁶, A. Rakitine⁴², M.S. Rangel², K. Ranjan²⁸, P.N. Ratoff⁴², P. Renkel⁷⁹, S. Reucroft⁶³, P. Rich⁴⁴, J. Rieger⁵⁴, M. Rijssenbeek⁷², I. Ripp-Baudot¹⁹, F. Rizatdinova⁷⁶, S. Robinson⁴³, R.F. Rodrigues³, M. Rominsky⁷⁵, C. Royon¹⁸, P. Rubinov⁵⁰, R. Ruchti⁵⁵, G. Safronov³⁷, G. Sajot¹⁴, A. Sánchez-Hernández³³, M.P. Sanders¹⁷, B. Sanghi⁵⁰, A. Santoro³, G. Savage⁵⁰, L. Sawyer⁶⁰, T. Scanlon⁴³, D. Schaile²⁵, R.D. Schamberger⁷², Y. Scheglov⁴⁰, H. Schellman⁵³, T. Schliephake²⁶, C. Schwanenberger⁴⁴, A. Schwartzman⁶⁸, R. Schwienhorst⁶⁵, J. Sekaric⁴⁹, H. Severini⁷⁵, E. Shabalina⁵¹, M. Shamim⁵⁹, V. Shary¹⁸, A.A. Shchukin³⁹, R.K. Shivpuri²⁸, V. Siccardi¹⁹, V. Simak¹⁰, V. Sirotenko⁵⁰, N.B. Skachkov³⁶, P. Skubic⁷⁵, P. Slattery⁷¹, D. Smirnov⁵⁵, G.R. Snow⁶⁷, J. Snow⁷⁴, S. Snyder⁷³, S. Söldner-Rembold⁴⁴, L. Sonnenschein¹⁷, A. Sopczak⁴², M. Sosebee⁷⁸, K. Soustruznik⁹, B. Spurlock⁷⁸, J. Stark¹⁴, J. Steele⁶⁰, V. Stolin³⁷, D.A. Stoyanova³⁹, J. Strandberg⁶⁴, S. Strandberg⁴¹, M.A. Strang⁶⁹, E. Strauss⁷², M. Strauss⁷⁵, R. Ströhmer²⁵, D. Strom⁵³, L. Stutte⁵⁰, S. Sumowidagdo⁴⁹, P. Svoisky⁵⁵, A. Sznajder³, P. Tamburello⁴⁵, A. Tanasijczuk¹, W. Taylor⁶, J. Temple⁴⁵, B. Tiller²⁵, F. Tissandier¹³, M. Titov¹⁸, V.V. Tokmenin³⁶, T. Toole⁶¹, I. Torchiani²³, T. Trefzger²⁴, D. Tsybychev⁷², B. Tuchming¹⁸, C. Tully⁶⁸, P.M. Tuts⁷⁰, R. Unalan⁶⁵, L. Uvarov⁴⁰, S. Uvarov⁴⁰, S. Uzunyan⁵², B. Vachon⁶, P.J. van den Berg³⁴, R. Van Kooten⁵⁴, W.M. van Leeuwen³⁴, N. Varelas⁵¹, E.W. Varnes⁴⁵, I.A. Vasilyev³⁹, M. Vaupel²⁶, P. Verdier²⁰, L.S. Vertogradov³⁶, M. Verzocchi⁵⁰, F. Villeneuve-Seguié⁴³, P. Vint⁴³, P. Vokac¹⁰, E. Von Toerne⁵⁹, M. Voutilainen^{68,e}, R. Wagner⁶⁸, H.D. Wahl⁴⁹, L. Wang⁶¹, M.H.L.S. Wang⁵⁰, J. Warchol⁵⁵, G. Watts⁸², M. Wayne⁵⁵, G. Weber²⁴, M. Weber⁵⁰, L. Welty-Rieger⁵⁴, A. Wenger^{23,f}, N. Wermes²², M. Wetstein⁶¹, A. White⁷⁸, D. Wicke²⁶, G.W. Wilson⁵⁸, S.J. Wimpenny⁴⁸, M. Wobisch⁶⁰, D.R. Wood⁶³, T.R. Wyatt⁴⁴, Y. Xie⁷⁷, S. Yacoob⁵³, R. Yamada⁵⁰, M. Yan⁶¹, T. Yasuda⁵⁰, Y.A. Yatsunenkov³⁶, K. Yip⁷³, H.D. Yoo⁷⁷, S.W. Youn⁵³, J. Yu⁷⁸, C. Zeitnitz²⁶, T. Zhao⁸², B. Zhou⁶⁴, J. Zhu⁷², M. Zielinski⁷¹, D. Zieminska⁵⁴, A. Zieminski^{54,†}, L. Zivkovic⁷⁰, V. Zutshi⁵², and E.G. Zverev³⁸

(The DØ Collaboration)

¹Universidad de Buenos Aires, Buenos Aires, Argentina

²LAFEX, Centro Brasileiro de Pesquisas Físicas, Rio de Janeiro, Brazil

³Universidade do Estado do Rio de Janeiro, Rio de Janeiro, Brazil

⁴Universidade Federal do ABC, Santo André, Brazil

⁵Instituto de Física Teórica, Universidade Estadual Paulista, São Paulo, Brazil

⁶University of Alberta, Edmonton, Alberta, Canada,

Simon Fraser University, Burnaby, British Columbia,

Canada, York University, Toronto, Ontario, Canada,

and McGill University, Montreal, Quebec, Canada

⁷University of Science and Technology of China, Hefei, People's Republic of China

⁸Universidad de los Andes, Bogotá, Colombia

⁹Center for Particle Physics, Charles University, Prague, Czech Republic

¹⁰Czech Technical University, Prague, Czech Republic

¹¹Center for Particle Physics, Institute of Physics, Academy of Sciences of the Czech Republic, Prague, Czech Republic

¹²Universidad San Francisco de Quito, Quito, Ecuador

¹³LPC, Univ Blaise Pascal, CNRS/IN2P3, Clermont, France

¹⁴LPSC, Université Joseph Fourier Grenoble 1, CNRS/IN2P3,

Institut National Polytechnique de Grenoble, France

¹⁵CPPM, Aix-Marseille Université, CNRS/IN2P3, Marseille, France

¹⁶LAL, Univ Paris-Sud, IN2P3/CNRS, Orsay, France

¹⁷LPNHE, IN2P3/CNRS, Universités Paris VI and VII, Paris, France

¹⁸DAPNIA/Service de Physique des Particules, CEA, Saclay, France

¹⁹IPHC, Université Louis Pasteur et Université de Haute Alsace, CNRS/IN2P3, Strasbourg, France

²⁰IPNL, Université Lyon 1, CNRS/IN2P3, Villeurbanne, France and Université de Lyon, Lyon, France

²¹III. Physikalisches Institut A, RWTH Aachen, Aachen, Germany

²²Physikalisches Institut, Universität Bonn, Bonn, Germany

²³Physikalisches Institut, Universität Freiburg, Freiburg, Germany

²⁴Institut für Physik, Universität Mainz, Mainz, Germany

²⁵Ludwig-Maximilians-Universität München, München, Germany

²⁶Fachbereich Physik, University of Wuppertal, Wuppertal, Germany

²⁷Panjab University, Chandigarh, India

²⁸Delhi University, Delhi, India

²⁹Tata Institute of Fundamental Research, Mumbai, India

- ³⁰ *University College Dublin, Dublin, Ireland*
- ³¹ *Korea Detector Laboratory, Korea University, Seoul, Korea*
- ³² *SungKyunKwan University, Suwon, Korea*
- ³³ *CINVESTAV, Mexico City, Mexico*
- ³⁴ *FOM-Institute NIKHEF and University of Amsterdam/NIKHEF, Amsterdam, The Netherlands*
- ³⁵ *Radboud University Nijmegen/NIKHEF, Nijmegen, The Netherlands*
- ³⁶ *Joint Institute for Nuclear Research, Dubna, Russia*
- ³⁷ *Institute for Theoretical and Experimental Physics, Moscow, Russia*
- ³⁸ *Moscow State University, Moscow, Russia*
- ³⁹ *Institute for High Energy Physics, Protvino, Russia*
- ⁴⁰ *Petersburg Nuclear Physics Institute, St. Petersburg, Russia*
- ⁴¹ *Lund University, Lund, Sweden, Royal Institute of Technology and Stockholm University, Stockholm, Sweden, and Uppsala University, Uppsala, Sweden*
- ⁴² *Lancaster University, Lancaster, United Kingdom*
- ⁴³ *Imperial College, London, United Kingdom*
- ⁴⁴ *University of Manchester, Manchester, United Kingdom*
- ⁴⁵ *University of Arizona, Tucson, Arizona 85721, USA*
- ⁴⁶ *Lawrence Berkeley National Laboratory and University of California, Berkeley, California 94720, USA*
- ⁴⁷ *California State University, Fresno, California 93740, USA*
- ⁴⁸ *University of California, Riverside, California 92521, USA*
- ⁴⁹ *Florida State University, Tallahassee, Florida 32306, USA*
- ⁵⁰ *Fermi National Accelerator Laboratory, Batavia, Illinois 60510, USA*
- ⁵¹ *University of Illinois at Chicago, Chicago, Illinois 60607, USA*
- ⁵² *Northern Illinois University, DeKalb, Illinois 60115, USA*
- ⁵³ *Northwestern University, Evanston, Illinois 60208, USA*
- ⁵⁴ *Indiana University, Bloomington, Indiana 47405, USA*
- ⁵⁵ *University of Notre Dame, Notre Dame, Indiana 46556, USA*
- ⁵⁶ *Purdue University Calumet, Hammond, Indiana 46323, USA*
- ⁵⁷ *Iowa State University, Ames, Iowa 50011, USA*
- ⁵⁸ *University of Kansas, Lawrence, Kansas 66045, USA*
- ⁵⁹ *Kansas State University, Manhattan, Kansas 66506, USA*
- ⁶⁰ *Louisiana Tech University, Ruston, Louisiana 71272, USA*
- ⁶¹ *University of Maryland, College Park, Maryland 20742, USA*
- ⁶² *Boston University, Boston, Massachusetts 02215, USA*
- ⁶³ *Northeastern University, Boston, Massachusetts 02115, USA*
- ⁶⁴ *University of Michigan, Ann Arbor, Michigan 48109, USA*
- ⁶⁵ *Michigan State University, East Lansing, Michigan 48824, USA*
- ⁶⁶ *University of Mississippi, University, Mississippi 38677, USA*
- ⁶⁷ *University of Nebraska, Lincoln, Nebraska 68588, USA*
- ⁶⁸ *Princeton University, Princeton, New Jersey 08544, USA*
- ⁶⁹ *State University of New York, Buffalo, New York 14260, USA*
- ⁷⁰ *Columbia University, New York, New York 10027, USA*
- ⁷¹ *University of Rochester, Rochester, New York 14627, USA*
- ⁷² *State University of New York, Stony Brook, New York 11794, USA*
- ⁷³ *Brookhaven National Laboratory, Upton, New York 11973, USA*
- ⁷⁴ *Langston University, Langston, Oklahoma 73050, USA*
- ⁷⁵ *University of Oklahoma, Norman, Oklahoma 73019, USA*
- ⁷⁶ *Oklahoma State University, Stillwater, Oklahoma 74078, USA*
- ⁷⁷ *Brown University, Providence, Rhode Island 02912, USA*
- ⁷⁸ *University of Texas, Arlington, Texas 76019, USA*
- ⁷⁹ *Southern Methodist University, Dallas, Texas 75275, USA*
- ⁸⁰ *Rice University, Houston, Texas 77005, USA*
- ⁸¹ *University of Virginia, Charlottesville, Virginia 22901, USA and*
- ⁸² *University of Washington, Seattle, Washington 98195, USA*

(Dated: April 7, 2008)

The process $p\bar{p} \rightarrow \gamma + \text{jet} + X$ is studied using 1.0 fb^{-1} of data collected by the D0 detector at the Fermilab Tevatron $p\bar{p}$ collider at a center-of-mass energy $\sqrt{s} = 1.96 \text{ TeV}$. Photons are reconstructed in the central rapidity region $|y^\gamma| < 1.0$ with transverse momenta in the range $30 < p_T^\gamma < 400 \text{ GeV}$ while jets are reconstructed in either the central $|y^{\text{jet}}| < 0.8$ or forward $1.5 < |y^{\text{jet}}| < 2.5$ rapidity intervals with $p_T^{\text{jet}} > 15 \text{ GeV}$. The differential cross section $d^3\sigma/dp_T^\gamma dy^\gamma dy^{\text{jet}}$ is measured as a function of p_T^γ in four regions, differing by the relative orientations of the photon and the jet in rapidity. Ratios between the differential cross sections in each region are also presented. Next-to-leading order QCD predictions using different parameterizations of parton distribution functions and theoretical scale

choices are compared to the data. The predictions do not simultaneously describe the measured normalization and p_T^γ dependence of the cross section in the four measured regions.

PACS numbers: 13.85.Qk, 12.38.Qk

The production of a photon with associated jets in the final state is a powerful probe of the dynamics of hard QCD interactions [1, 2, 3, 4, 5, 6]. Different angular configurations between the photon and the jets can be used to extend inclusive photon production measurements [7, 8, 9, 10] and simultaneously test the underlying dynamics of QCD hard-scattering subprocesses in different regions of parton momentum fraction x and large hard-scattering scales Q^2 .

In this Letter, we present an analysis of photon plus jets production in $p\bar{p}$ collisions at a center-of-mass energy $\sqrt{s}=1.96$ TeV in which the most-energetic (leading) photon is produced centrally with a rapidity $|y^\gamma| < 1.0$ [11]. The cross section as a function of photon transverse momentum p_T^γ is measured differentially for four separate angular configurations of the highest p_T (leading) jet and the leading photon rapidities. The leading jet is required to be in either the central ($|y^{\text{jet}}| < 0.8$) or forward ($1.5 < |y^{\text{jet}}| < 2.5$) rapidity intervals, with $p_T^{\text{jet}} > 15$ GeV, and the four angular configurations studied are: central jets with $y^\gamma \cdot y^{\text{jet}} > 0$ and with $y^\gamma \cdot y^{\text{jet}} < 0$, and forward jets with $y^\gamma \cdot y^{\text{jet}} > 0$ and with $y^\gamma \cdot y^{\text{jet}} < 0$. The total x and Q^2 region covered by the measurement is $0.007 \lesssim x \lesssim 0.8$ and $900 \leq Q^2 \equiv (p_T^\gamma)^2 \leq 1.6 \times 10^5$ GeV², extending the kinematic reach of previous photon plus jet measurements [12, 13, 14, 15, 16, 17, 18]. Ratios between the differential cross sections in the four studied angular configurations are also presented. The measurements are compared to the corresponding theoretical predictions.

Isolated final-state photons produced in $p\bar{p} \rightarrow \gamma + \text{jet} + X$ events are expected to mainly originate “directly” from QCD Compton-like $qg \rightarrow q\gamma$ scattering or $q\bar{q} \rightarrow g\gamma$ annihilation subprocesses. In Fig. 1 the expected contribution, estimated using PYTHIA [19] Monte Carlo (MC) event generator with the CTEQ6.5M parton distribution function (PDF) set [20], of the Compton-like partonic scattering process to the total associated production of a photon and a jet is shown for each of the four measured rapidity intervals. The parton distribution functions entering into the theoretical predictions have substantial uncertainties, particularly for the gluon contributions at small x , large x and large Q^2 [20, 21]. The measurement intervals probe different regions of parton momentum-fraction space of the two initial interacting partons, $x_{1,2}$. For example at $p_T^{\text{jet}} = 40$ GeV, in events with a central leading jet, the $y^\gamma \cdot y^{\text{jet}} > 0$ region covers adjacent x_1 and x_2 intervals ($0.016 \lesssim x_1 \lesssim 0.040$ and $0.040 \lesssim x_2 \lesssim 0.100$), while for events with $y^\gamma \cdot y^{\text{jet}} < 0$, the x_1 and x_2 intervals are similar ($0.029 \lesssim x_1 \lesssim 0.074$, $0.027 \lesssim x_2 \lesssim 0.065$). In events with a forward leading jet, intervals of small and large x are covered ($0.009 \lesssim$

$x_1 \lesssim 0.024$, $0.110 \lesssim x_2 \lesssim 0.300$ for $y^\gamma \cdot y^{\text{jet}} > 0$ and $0.097 \lesssim x_1 \lesssim 0.264$, $0.022 \lesssim x_2 \lesssim 0.059$ for $y^\gamma \cdot y^{\text{jet}} < 0$). Here $x_{1,2}$ are defined using the leading order approximation $x_{1,2} = (p_T^\gamma/\sqrt{s})(e^{\pm y^\gamma} + e^{\pm y^{\text{jet}}})$ [1, 2, 3, 4, 5, 6].

The data presented here correspond to an integrated luminosity of 1.01 ± 0.06 fb⁻¹ [22] collected using the D0 detector at the Fermilab Tevatron $p\bar{p}$ collider operating at a center-of-mass energy $\sqrt{s} = 1.96$ TeV. A detailed description of the D0 detector can be found in [23] and only an overview of the detector components relevant to this analysis is given here.

Photon candidates are formed from clusters of calorimeter cells in the central part of the liquid-argon and uranium calorimeter. The central calorimeter covers the pseudorapidity range $|\eta| < 1.1$ and two end calorimeters cover $1.5 < |\eta| < 4.2$ [24]. The electromagnetic (EM) section of the central calorimeter contains four longitudinal layers of 2, 2, 7, and 10 radiation lengths, and is finely-segmented transversely into cells of size $\Delta\eta \times \Delta\phi = 0.1 \times 0.1$ (0.05×0.05 in the third EM layer), providing good angular resolution for photons and electrons. The position and width of the Z boson mass peak, reconstructed from $Z \rightarrow e^+e^-$ events, are used to determine the EM calorimeter calibration factors and the EM energy resolution [25]. The central section of the calorimeter surrounds a central preshower detector, with three concentric cylindrical layers of scintillator strips, and a tracking system consisting of silicon microstrip and

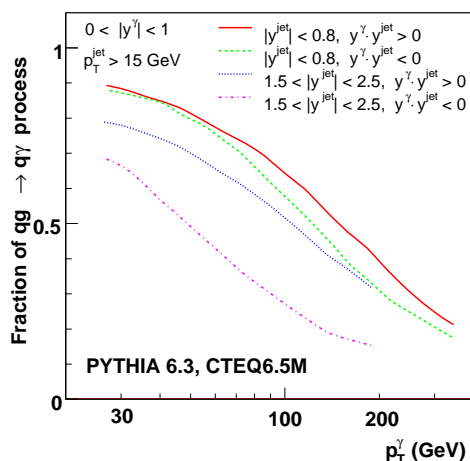


FIG. 1: The fraction of events, estimated using the PYTHIA event generator, produced via the $qg \rightarrow q\gamma$ subprocess relative to the total associated production of a direct photon and a jet for each of the four measured configurations of the leading jet and leading photon rapidities.

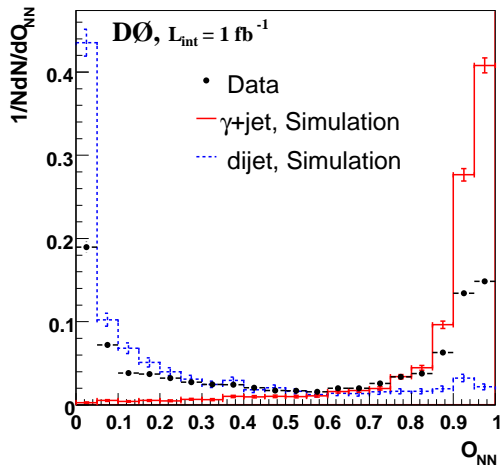


FIG. 2: Normalized distribution of the ANN output O_{NN} for data, $\gamma + \text{jet}$ signal MC, and dijet background MC events for $44 < p_T^\gamma < 50$ GeV after application of the main selection criteria.

scintillating fiber trackers located within a 2 T solenoidal magnetic field.

The D0 tracking system is used to select events which contain a primary collision vertex, reconstructed with at least three tracks, within 50 cm of the center of the detector along the beam axis. The efficiency of the vertex requirement varies as a function of instantaneous luminosity from 92% to 96%.

Photon candidates with rapidity $|y^\gamma| < 1.0$ are selected from clusters of calorimeter cells within a cone of radius $\mathcal{R} \equiv \sqrt{(\Delta\eta)^2 + (\Delta\phi)^2} = 0.4$ defined around a seed tower [23]. The final cluster energy is then re-calculated from the inner cone with $\mathcal{R} = 0.2$. The data are selected using a combination of triggers based on photon EM shower profiles in the calorimeter and EM cluster p_T thresholds. The total trigger efficiency is (96–97)% for photon candidates with $p_T^\gamma \approx 32$ GeV and greater than 99% for $p_T^\gamma > 40$ GeV. The selected clusters are required to have greater than 96% of their total energy contained in the EM calorimeter layers. Isolated clusters are selected by requiring that the energy $E_{EM}(\mathcal{R} = 0.2)$, calculated within the inner cone of radius $\mathcal{R} = 0.2$, fulfills the condition $[E_{total}(\mathcal{R} = 0.4) - E_{EM}(\mathcal{R} = 0.2)]/E_{EM}(\mathcal{R} = 0.2) < 0.07$, where $E_{total}(\mathcal{R} = 0.4)$ is the summed EM and hadronic energy within a cone of radius $\mathcal{R} = 0.4$. The candidate EM cluster is required not to be spatially matched to a reconstructed track. This is accomplished by computing a χ^2 function evaluating the consistency, within uncertainties, between the reconstructed η and ϕ positions of the cluster and the closest track in the finely-segmented third layer of the EM calorimeter. The corresponding χ^2 probability is required to be $< 0.1\%$. Background contributions to the direct photon sample from cosmic rays and from isolated electrons, originating from the leptonic decays of W bosons, important

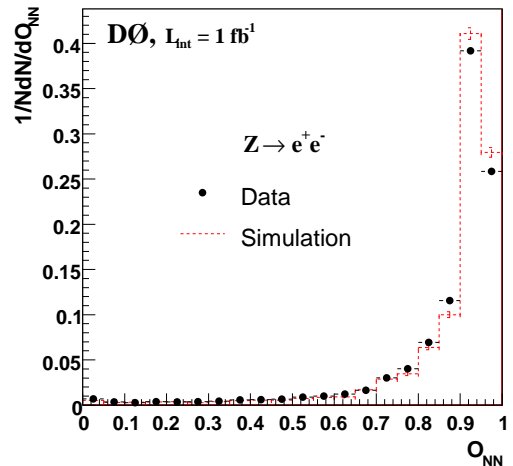


FIG. 3: Normalized distribution of the ANN output O_{NN} for electrons from Z^0 boson decays in data and MC events.

at high p_T^γ [26], are suppressed by requiring the missing transverse energy \cancel{E}_T , calculated as a vector sum of the transverse energies of all calorimeter cells, to satisfy the condition $\cancel{E}_T < 12.5 + 0.36 p_T^\gamma$ GeV. The longitudinal segmentation of the EM calorimeter and central preshower detector allow us to estimate the photon candidate direction and vertex coordinate along the beam axis (“photon vertex pointing”). This vertex is required to lie within 10 cm of the event primary vertex reconstructed from charged particles.

Photons arising from decays of π^0 and η mesons are already largely suppressed by the requirements above, and especially by photon isolation, since these mesons are produced mainly within jets during fragmentation and are surrounded by other particles. To better select photons and estimate the residual background, an artificial neural network (ANN) is constructed using the JETNET package [27]. The following three variables are used in the ANN: the number of cells in the first EM layer belonging to the cluster, the fraction of the cluster energy deposited in the first EM layer, and the scalar sum of charged particle transverse momenta in the hollow cone $0.05 \leq \mathcal{R} \leq 0.4$ around the photon cluster direction. The resulting ANN output, O_{NN} , after applying all data selection criteria, is shown, normalized to unit area, in Fig. 2 for $44 < p_T^\gamma < 50$ GeV. The output is compared to photon signal events and dijet background events simulated using PYTHIA. The signal events may contain photons originating from the parton-to-photon fragmentation process. For this reason, the background events, produced with QCD processes in PYTHIA, were preselected to exclude the bremsstrahlung photons produced from partons. Signal and background MC events were processed through a GEANT-based [28] simulation of the D0 detector and the same reconstruction code as used for the data. The ANN is tested using electrons from

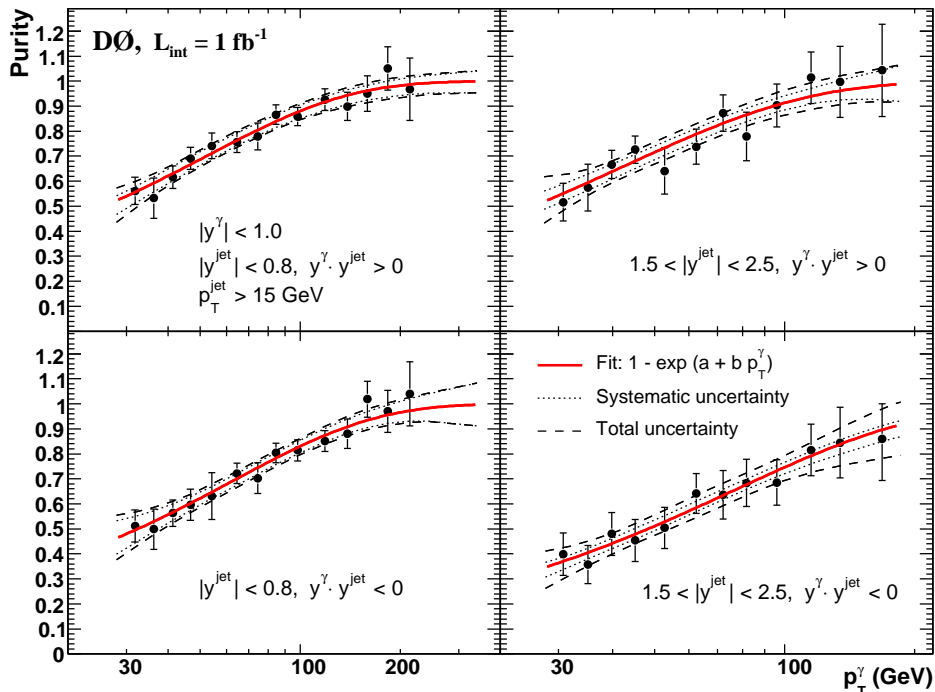


FIG. 4: The purity of the selected $p\bar{p} \rightarrow \gamma + \text{jet} + X$ sample as a function of p_T^γ for each measured configuration of photon and jet rapidities. The results of the $1 - \exp(a + bp_T^\gamma)$ functional fits are shown by the solid lines, together with the systematic uncertainties (dotted lines), and the total uncertainties (dashed lines).

Z boson decays and the resulting normalized data and MC distributions are compared in Fig. 3. Photon candidates are selected by the requirement $O_{\text{NN}} > 0.7$ which has good background rejection and a signal efficiency in the range (93–97)%. The signal selection efficiency decreases by about 4% with increasing p_T^γ from 30 GeV to 300 GeV due to the $O_{\text{NN}} > 0.7$ requirement. The total photon+jet selection efficiency after applying all the selection criteria, including the ANN and the \cancel{E}_T requirements, is (63–77)% as a function of p_T^γ with an overall systematic uncertainty of (4.7–5.2)%. Main sources of inefficiency are the isolation, anti-track matching, ANN, and the photon vertex pointing cuts.

Events containing at least one hadronic jet are selected. Jets are reconstructed using the D0 Run II jet-finding algorithm with a cone of radius 0.7 [29], and are required to satisfy quality criteria which suppress background from leptons, photons, and detector noise effects. Jet energies are corrected to the particle level. The leading jet should have $p_T^{\text{jet}} > 15$ GeV and $|y^{\text{jet}}| < 0.8$ or $1.5 < |y^{\text{jet}}| < 2.5$. The leading photon candidate and the leading jet are also required to be separated in $\eta - \phi$ space by $\Delta\mathcal{R}(\gamma, \text{jet}) > 0.7$. The leading jet total selection efficiency varies from 94% to almost 100% and takes into account any migrations between leading and second jet from the particle to the reconstruction level. The total systematic uncertainty on this efficiency is 5.7% at $p_T^\gamma \simeq 30$ GeV, decreasing to about 2% at $p_T^\gamma \geq 200$ GeV. The measurement is not

very sensitive to jet energy scale corrections since it is performed in bins of p_T^γ (with $p_T^\gamma > 30$ GeV) and only information on the the jet angular direction is used.

In total, about 1.4 million candidate events are selected after application of all selection criteria. A correction for the “ γ +jet” event purity \mathcal{P} is then applied to account for the remaining background in the region $O_{\text{NN}} > 0.7$. The distribution of the ANN output for the simulated photon signal and dijet background samples are fitted to the data for each p_T^γ bin using a maximum likelihood fit [30] to obtain the fractions of signal and background components in the data without constraining the fractions of signal and background samples in the fit to be in the [0, 1] range. The data and fitted sum of the weighted signal and background MC distributions of O_{NN} are found to be compatible with χ^2/ndf values in the range 0.2–1.3 [31]. The resulting purities are shown in Fig. 4 for each measurement region. The p_T^γ dependence of the purity is fitted in each region using a two parameter function $\mathcal{P} = 1 - \exp(a + bp_T^\gamma)$. The result of the fits together with their statistical errors are shown in Fig. 4. The systematic uncertainties on the fit are estimated using alternative fitting functions and varying the number of bins in the fitting of the ANN output distribution. An additional systematic uncertainty due to the fragmentation model implemented in PYTHIA is also taken into account. It is found to be 5% at $p_T^\gamma \simeq 30$ GeV, 2% at $p_T^\gamma \simeq 50$ GeV, and 1% at $p_T^\gamma \gtrsim 70$ GeV [10].

To study whether bremsstrahlung photons have different selection efficiencies from direct photons, we extracted them from dijet events simulated with PYTHIA. We found that they do not produce a noticeable change of the selection efficiencies, acceptance and shape of the photon ANN output that have been obtained with direct photons.

The differential cross section $d^3\sigma/dp_T^\gamma dy^\gamma dy^{\text{jet}}$ for the process $p\bar{p} \rightarrow \gamma + \text{jet} + X$ is obtained from the number of data events in each interval, after applying corrections for background, efficiency, and acceptance effects, divided by the integrated luminosity and the widths of the interval in the photon transverse momentum, photon rapidity, and jet rapidity. The data are also corrected for p_T bin-migration effects which result from the finite energy resolution of the EM calorimeter using an analytical Ansatz method [33] and the measured EM energy resolution determined from the Z boson peak. The correction factors range from (1–5)% with about a 1% uncertainty.

The total ($\delta\sigma_{\text{tot}}^{\text{exp}}$) and main sources of experimental systematic uncertainty are shown for the $|y^{\text{jet}}| < 0.8$, $y^\gamma \cdot y^{\text{jet}} > 0$ region in Fig. 5. Similar uncertainties are found for the other measured regions. The largest uncertainties are assigned to the purity estimation [(10–4)%], photon and jet selections [(7.7–5.2)%], photon energy scale [(4.2–6.0)%], and the integrated luminosity (6.1%). The uncertainty ranges above are quoted with uncertainty at low p_T^γ first and at high p_T^γ second. The systematic uncertainty on the photon selection is due mainly to the anti-track match cut (3%), a correction due to observed data/MC difference in the efficiency of the main photon selection criteria found from $Z \rightarrow ee$ events [(1.5–2)%], the photon vertex pointing requirement (2%), the ANN cut (2%), and the uncertainty on the parameterized photon selection efficiency (<1%). The total experimental systematic uncertainty for each data point is obtained by adding all the individual contributions in quadrature.

The result for each region is presented as a function

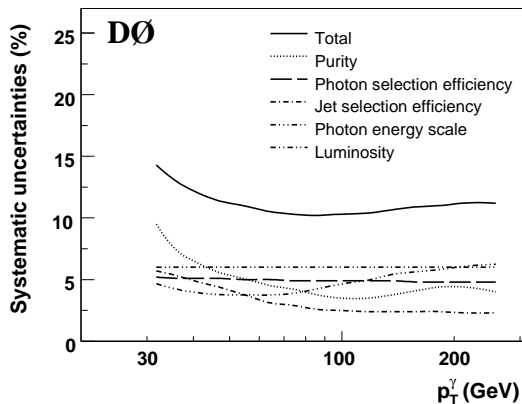


FIG. 5: The total and main sources of systematic uncertainty for the cross section measured in the $|y^{\text{jet}}| < 0.8$, $y^\gamma \cdot y^{\text{jet}} > 0$ rapidity region.

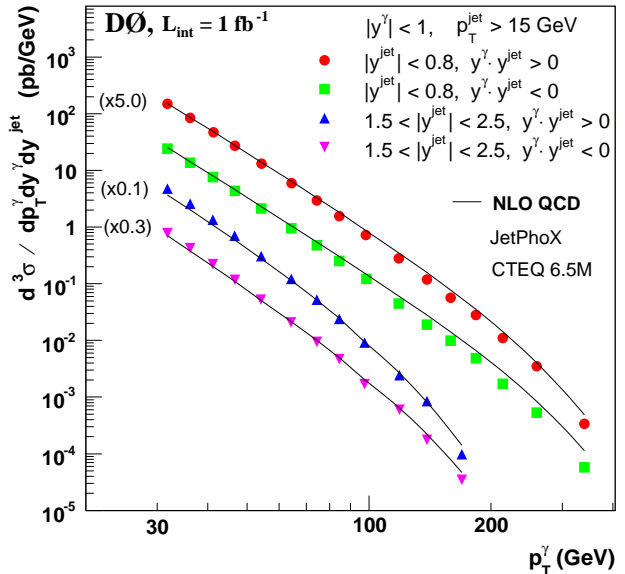


FIG. 6: The measured differential $p\bar{p} \rightarrow \gamma + \text{jet} + X$ cross section as a function of p_T^γ for the four measured rapidity intervals. For presentation purposes, the cross section results for central ($|y^{\text{jet}}| < 0.8$) jets with $y^\gamma \cdot y^{\text{jet}} > 0$ and for forward ($1.5 < |y^{\text{jet}}| < 2.5$) jets with $y^\gamma \cdot y^{\text{jet}} > 0$ and $y^\gamma \cdot y^{\text{jet}} < 0$ are scaled by factors of 5, 0.1 and 0.3, respectively. The data are compared to the theoretical NLO QCD predictions using the JETPHOX package [36] with the CTEQ6.5M PDF set [20] and renormalization, factorization and fragmentation scales $\mu_R = \mu_F = \mu_f = p_T^\gamma f(y^*)$.

TABLE I: Differential cross sections $d^3\sigma/dp_T^\gamma dy^\gamma dy^{\text{jet}}$ and uncertainties for the $|y^{\text{jet}}| < 0.8$, $y^\gamma \cdot y^{\text{jet}} > 0$ rapidity interval.

p_T^γ bin (GeV)	$\langle p_T^\gamma \rangle$ (GeV)	Cross section (pb/GeV)	$\delta\sigma_{\text{stat}}$ (%)	$\delta\sigma_{\text{syst}}$ (%)	$\delta\sigma_{\text{tot}}^{\text{exp}}$ (%)
30 – 34	31.9	3.08×10^1	0.2	14.2	14.2
34 – 39	36.3	1.74×10^1	0.3	13.1	13.1
39 – 44	41.3	9.76×10^0	0.4	12.4	12.4
44 – 50	46.8	5.60×10^0	0.5	11.9	11.9
50 – 60	54.6	2.76×10^0	0.6	11.5	11.5
60 – 70	64.6	1.24×10^0	0.9	11.0	11.0
70 – 80	74.7	6.25×10^{-1}	1.2	10.8	10.9
80 – 90	84.7	3.32×10^{-1}	1.7	10.6	10.7
90 – 110	99.0	1.51×10^{-1}	1.8	10.6	10.7
110 – 130	119.1	5.79×10^{-2}	2.9	10.5	10.9
130 – 150	139.2	2.56×10^{-2}	4.3	10.7	11.5
150 – 170	159.3	1.17×10^{-2}	6.5	10.9	12.7
170 – 200	183.6	5.80×10^{-3}	7.6	11.0	13.3
200 – 230	213.8	2.33×10^{-3}	11.8	11.0	16.1
230 – 300	259.5	7.25×10^{-4}	13.8	10.7	17.5
300 – 400	340.5	7.96×10^{-5}	35.3	10.9	36.9

of p_T^γ in Fig. 6 and Tables I–IV. The data points are plotted at the value $\langle p_T^\gamma \rangle$ for which a value of the smooth function describing the cross section equals the average cross section in the bin [34]. The data cover six orders of magnitude in the cross section for events with $|y^{\text{jet}}| < 0.8$, falling more rapidly for four orders of magnitude for events with $1.5 < |y^{\text{jet}}| < 2.5$.

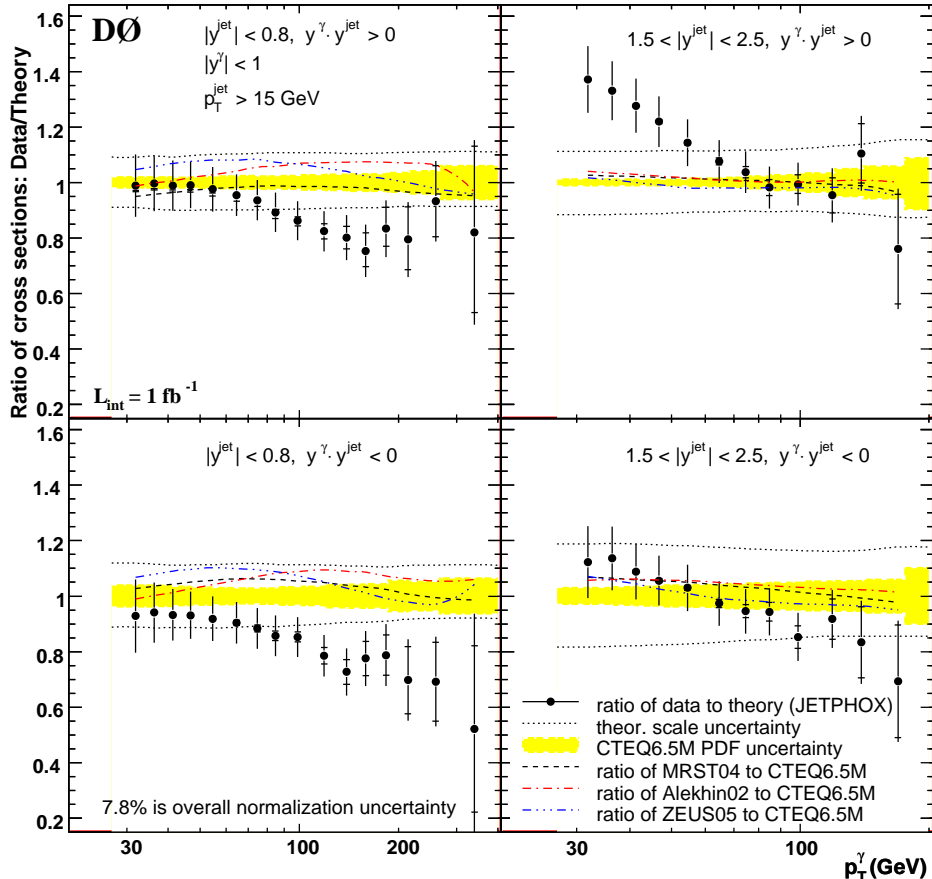


FIG. 7: The ratios of the measured triple-differential cross section, in each measured interval, to the NLO QCD prediction using JETPHOX [36] with the CTEQ6.5M PDF set and all three scales $\mu_{R,F,f} = p_T^\gamma f(y^*)$. The solid vertical line on the points shows the statistical and p_T -dependent systematic uncertainties added in quadrature, while the internal line shows the statistical uncertainty. The two dotted lines represent the effect of varying the theoretical scales by a factor of two. The shaded region is the CTEQ6.5M PDF uncertainty. The dashed and dash-dotted lines show ratios of the JETPHOX predictions with MRST 2004, Alekhin, and ZEUS 2005 to CTEQ6.5M PDF sets. Systematic uncertainties have large ($> 80\%$) p_T^γ bin-to-bin correlations. There is a common 7.8% normalization uncertainty that is not shown on the data points.

The data are compared to next-to-leading order (NLO) QCD predictions obtained using JETPHOX [35, 36], with CTEQ6.5M PDF [20] and BFG fragmentation functions of partons to photons [37]. The renormalization, factorization, and fragmentation scales (μ_R , μ_F , and μ_f) are set equal to $p_T^\gamma f(y^*)$, where $f(y^*) = \{[1 + \exp(-2|y^*|)]/2\}^{1/2}$ and $y^* = 0.5(y^\gamma - y^{\text{jet}})$ [38]. The theoretical predictions include selection criteria on the photon and jet similar to those applied in the experimental analysis. In particular, an isolation requirement on the photon of $[E_{\text{total}}(\mathcal{R} = 0.4) - E^\gamma]/E^\gamma < 0.07$ is made, where $E_{\text{total}}(\mathcal{R} = 0.4)$ is the total energy around the photon in a cone of radius $\mathcal{R} = 0.4$, and E^γ is the photon energy. This requirement suppresses the relative contribution from photons produced in the fragmentation process, and leads to a more consistent comparison with the experimental result. Corrections for the underlying

event and parton-to-hadron fragmentation contributions, estimated using PYTHIA, are found to be negligibly small and are not included. To make a more detailed comparison, the ratio of the measured cross section to the NLO QCD prediction is taken in each interval and the results are shown in Fig. 7. The inner error bars reflect the statistical uncertainty only, and the outer error bars are the total statistical and p_T -dependent systematic uncertainties summed in quadrature. Most of these systematic uncertainties, associated with the parametrizations of the photon and jet selection efficiencies, purity (including the uncertainty from the PYTHIA fragmentation model), photon p_T correction, and calorimeter energy scale, have large ($> 80\%$) bin-to-bin correlations in p_T^γ . Systematic p_T^γ -independent uncertainties from the luminosity measurement, photon selection efficiency caused by the anti-track matching, ANN and photon vertex pointing, ac-

TABLE II: Differential cross sections $d^3\sigma/dp_T^\gamma dy^\gamma dy^{\text{jet}}$ and uncertainties for the $|y^{\text{jet}}| < 0.8$, $y^\gamma \cdot y^{\text{jet}} < 0$ rapidity interval.

p_T^γ bin (GeV)	$\langle p_T^\gamma \rangle$ (GeV)	Cross section (pb/GeV)	$\delta\sigma_{\text{stat}}$ (%)	$\delta\sigma_{\text{syst}}$ (%)	$\delta\sigma_{\text{tot}}^{\text{exp}}$ (%)
30 – 34	31.9	2.51×10^1	0.3	15.7	15.7
34 – 39	36.3	1.42×10^1	0.3	13.9	13.9
39 – 44	41.3	7.90×10^0	0.4	12.6	12.6
44 – 50	46.8	4.48×10^0	0.5	11.9	11.9
50 – 60	54.6	2.20×10^0	0.6	11.5	11.5
60 – 70	64.6	9.99×10^{-1}	0.9	11.1	11.1
70 – 80	74.7	4.98×10^{-1}	1.3	10.9	11.0
80 – 90	84.7	2.67×10^{-1}	1.8	10.7	10.9
90 – 110	99.0	1.26×10^{-1}	1.9	10.7	10.9
110 – 130	119.1	4.74×10^{-2}	3.1	10.6	11.1
130 – 150	139.2	2.07×10^{-2}	4.7	10.9	11.9
150 – 170	159.3	1.08×10^{-2}	6.6	11.2	13.0
170 – 200	183.6	5.23×10^{-3}	7.7	11.7	14.0
200 – 230	213.8	1.90×10^{-3}	13.0	11.6	17.4
230 – 300	259.5	5.93×10^{-4}	15.0	11.2	18.7
300 – 400	340.5	5.32×10^{-5}	46.1	12.9	47.8

TABLE III: Differential cross sections $d^3\sigma/dp_T^\gamma dy^\gamma dy^{\text{jet}}$ and uncertainties for the $1.5 < |y^{\text{jet}}| < 2.5$, $y^\gamma \cdot y^{\text{jet}} > 0$ rapidity interval.

p_T^γ bin (GeV)	$\langle p_T^\gamma \rangle$ (GeV)	Cross section (pb/GeV)	$\delta\sigma_{\text{stat}}$ (%)	$\delta\sigma_{\text{syst}}$ (%)	$\delta\sigma_{\text{tot}}^{\text{exp}}$ (%)
30 – 34	31.9	1.67×10^1	0.3	14.7	14.7
34 – 39	36.3	8.74×10^0	0.4	13.5	13.5
39 – 44	41.3	4.53×10^0	0.5	12.8	12.8
44 – 50	46.8	2.36×10^0	0.7	12.4	12.4
50 – 60	54.5	1.02×10^0	0.8	11.8	11.8
60 – 70	64.6	3.96×10^{-1}	1.4	11.2	11.3
70 – 80	74.6	1.71×10^{-1}	2.1	10.8	11.0
80 – 90	84.7	7.76×10^{-2}	3.2	10.8	11.3
90 – 110	98.8	3.05×10^{-2}	3.6	10.7	11.3
110 – 130	118.9	8.27×10^{-3}	6.9	11.0	13.0
130 – 150	139.0	2.85×10^{-3}	11.8	11.5	16.5
150 – 200	169.4	3.15×10^{-4}	23.0	12.1	26.0

ceptance (1.5%), and unfolding (1%) lead to a total 7.8% overall normalization uncertainty and are not shown in Fig. 7.

The prediction using the CTEQ6.5M PDF and BGF fragmentation sets does not describe the shape of the cross section over the whole measured range. In particular, the prediction is above the data for events with $|y^{\text{jet}}| < 0.8$ in the region $p_T^\gamma > 100$ GeV and below the data for jets produced in the $1.5 < |y^{\text{jet}}| < 2.5$, $y^\gamma \cdot y^{\text{jet}} > 0$ rapidity region for $p_T^\gamma < 50$ GeV. Most of the data points

TABLE IV: Differential cross sections $d^3\sigma/dp_T^\gamma dy^\gamma dy^{\text{jet}}$ and uncertainties for the $1.5 < |y^{\text{jet}}| < 2.5$, $y^\gamma \cdot y^{\text{jet}} < 0$ rapidity interval.

p_T^γ bin (GeV)	$\langle p_T^\gamma \rangle$ (GeV)	Cross section (pb/GeV)	$\delta\sigma_{\text{stat}}$ (%)	$\delta\sigma_{\text{syst}}$ (%)	$\delta\sigma_{\text{tot}}^{\text{exp}}$ (%)
30 – 34	31.9	8.08×10^0	0.4	15.6	15.6
34 – 39	36.3	4.36×10^0	0.4	14.2	14.2
39 – 44	41.3	2.23×10^0	0.6	13.0	13.0
44 – 50	46.8	1.16×10^0	0.8	12.3	12.3
50 – 60	54.5	5.28×10^{-1}	1.0	11.7	11.7
60 – 70	64.6	2.08×10^{-1}	1.7	11.3	11.4
70 – 80	74.6	9.18×10^{-2}	2.6	11.2	11.5
80 – 90	84.7	4.61×10^{-2}	3.7	11.3	11.9
90 – 110	98.8	1.64×10^{-2}	4.5	11.2	12.1
110 – 130	118.9	5.31×10^{-3}	8.2	11.1	13.8
130 – 150	139.0	1.79×10^{-3}	14.1	11.2	18.0
150 – 200	169.4	3.04×10^{-4}	23.0	11.3	25.6

in these p_T^γ and rapidity regions are (1–1.5) $\delta\sigma_{\text{tot}}$ outside of the CTEQ6.5M PDF set uncertainty range which is shown by the shaded region in the figure and calculated according to the prescription in [20]. Note that the data-to-theory ratios have a shape similar to those observed in the inclusive photon cross sections measured by the UA2 [7], CDF [8] and D0 [10] collaborations.

The dotted lines in Fig. 7 show the effect of setting the renormalization, factorization, and fragmentation scales to $0.5p_T^\gamma f(y^*)$ (upper dotted line) and $2p_T^\gamma f(y^*)$ (lower dotted line). The effect on the normalization is (9–11)%, except for jets in the $1.5 < |y^{\text{jet}}| < 2.5$, $y^\gamma \cdot y^{\text{jet}} < 0$ rapidity range where it is (18–20)%. The scale variation is not able to simultaneously accommodate the measured differential cross sections in all of the measured regions. The ratios of the NLO QCD prediction with the MRST 2004 [39], Alekhin [40], and ZEUS 2005 [41] PDF sets to the prediction obtained using the CTEQ6.5M PDF set are also presented in the figure. The shapes of the predictions are very similar, especially for forward jet production, with the different PDF sets.

The ratios of the predicted cross sections with the default scales [$\mu_R = \mu_F = \mu_f = p_T^\gamma f(y^*)$] to those with all the scales set equal to p_T^γ are presented for each of the four kinematic regions as a function of p_T^γ in Fig. 8. For each measured region, the new prediction is smaller than the default case across the entire p_T^γ range, most notably in the forward jet rapidity intervals where this choice of scale leads to a poorer level of agreement between data and theory.

Uncertainties related to the photon production due to the fragmentation mechanism are also studied separately using the JETPHOX package. The ratio of the $p\bar{p} \rightarrow \gamma + \text{jet} + X$ cross section for the direct photon contribution to the sum of direct and fragmentation contributions is shown, for the chosen photon isolation criteria, in each of the four measured regions in Fig. 9. For all regions, the fragmentation contribution decreases with increasing p_T^γ [35, 42, 43] and is largest for the $1.5 < |y^{\text{jet}}| < 2.5$, $y^\gamma \cdot y^{\text{jet}} < 0$ region. A variation in the fragmentation scale by a factor of four leads to only a (2–3)% change in the total predicted cross section. Similarly a change in default set of fragmentation functions (BFG Set 1 to BFG Set 2) results in a cross section change of $\lesssim 1\%$.

A possible contribution to the theoretical cross section from threshold resummation has been estimated [44] for inclusive direct photon production at the Tevatron and found to be $\lesssim (2.5 - 3.0)\%$ for $p_T^\gamma \lesssim 350$ GeV.

The experimental systematic uncertainties are reduced further by measuring the ratios between the differential cross sections $D = d^3\sigma/dp_T^\gamma dy^\gamma dy^{\text{jet}}$ in the differential regions. Most of the systematic uncertainties related to the identification of central photons then cancel, and only systematic uncertainties related to the $p\bar{p} \rightarrow \gamma + \text{jet} + X$ event purities and the jet selection efficiency (when measuring ratios between central and forward jet

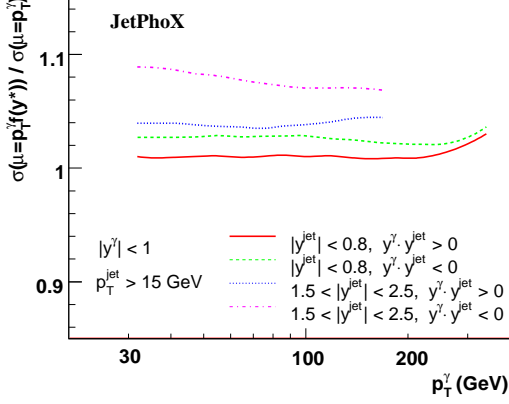


FIG. 8: Ratio of the predicted cross section with $\mu_{R,F,f} = p_T^\gamma f(y^*)$ to those with $\mu_{R,F,f} = p_T^\gamma$ in each measured region.

regions) remain. Measured ratios between the differential cross sections in the different regions are presented in Fig. 10 and Tables V–X. The overall experimental uncertainty is largest in the first and last p_T^γ bins and ranges from (3–9)% across most of the p_T^γ range. The NLO QCD predicted cross section ratios estimated using JETPHOX are also presented for scale choices $\mu_{R,F,f} = p_T^\gamma f(y^*)$, $\mu_{R,F,f} = 0.5p_T^\gamma f(y^*)$, and $\mu_{R,F,f} = 2p_T^\gamma f(y^*)$. The scale uncertainty of the predicted ratios is $\leq 3\%$ and about (3.5–7.5)% for the ratio of cross sections in the two forward jet rapidity intervals. The shapes of the measured ratios between the cross sections in the different regions, in general, are qualitatively reproduced by the theory. A quantitative difference, however, between theory and the measurement is observed for the ratios of the central jet regions to the forward $1.5 < |y^{\text{jet}}| < 2.5, y^\gamma \cdot y^{\text{jet}} > 0$ region, even after the theoretical scale variation is taken into account. The ratio between the two forward jet cross sections suggests a scale choice $\mu_{R,F,f} \simeq 2p_T^\gamma f(y^*)$. However, the ratios of the central jet regions to the forward $1.5 < |y^{\text{jet}}| < 2.5, y^\gamma \cdot y^{\text{jet}} < 0$ region suggest a theoretical scale closer to $\mu_{R,F,f} \simeq 0.5p_T^\gamma f(y^*)$.

In summary, the differential cross section $d^3\sigma/dp_T^\gamma dy^\gamma dy^{\text{jet}}$ for the process $p\bar{p} \rightarrow \gamma + \text{jet} + X$ is measured for central photons ($|y^\gamma| < 1.0$) separately for four different rapidity configurations between the leading photon and the leading jet. The data cover six orders of magnitude in the cross section as a function of p_T^γ for events with jets in $|y^{\text{jet}}| < 0.8$, and extend the kinematic reach of previous photon plus jet measurements. Next-to-leading order QCD predictions, using a few different modern parameterizations of parton distribution functions, are unable to describe the shape of the p_T^γ dependence of the cross section across the entire measured range. Similarly, theoretical scale variations are unable to simultaneously describe the data-to-theory ratios in each of the four measured regions. Thus,

TABLE V: Ratios of the differential cross sections in the $|y^{\text{jet}}| < 0.8, y^\gamma \cdot y^{\text{jet}} < 0$ rapidity region to the $|y^{\text{jet}}| < 0.8, y^\gamma \cdot y^{\text{jet}} > 0$ rapidity region.

p_T^γ bin (GeV)	Ratio (r)	δr_{stat} (%)	δr_{syst} (%)	$\delta r_{\text{tot}}^{\text{exp}}$ (%)
30 – 34	0.81	0.4	9.1	9.1
34 – 39	0.81	0.4	7.8	7.8
39 – 44	0.81	0.6	6.0	6.0
44 – 50	0.80	0.7	4.8	4.8
50 – 60	0.80	0.8	3.7	3.8
60 – 70	0.81	1.3	3.1	3.3
70 – 80	0.80	1.8	2.9	3.4
80 – 90	0.81	2.5	2.8	3.8
90 – 110	0.83	2.6	2.8	3.8
110 – 130	0.82	4.3	2.7	5.0
130 – 150	0.81	6.4	2.4	6.9
150 – 170	0.93	9.3	2.2	9.5
170 – 200	0.90	10.8	2.1	11.0
200 – 230	0.81	17.6	2.0	17.7
230 – 300	0.82	20.4	1.8	20.4
300 – 400	0.67	58.0	0.1	58.0

TABLE VI: Ratios of the differential cross sections in the $|y^{\text{jet}}| < 0.8, y^\gamma \cdot y^{\text{jet}} > 0$ rapidity region to the $1.5 < |y^{\text{jet}}| < 2.5, y^\gamma \cdot y^{\text{jet}} > 0$ rapidity region.

p_T^γ bin (GeV)	Ratio (r)	δr_{stat} (%)	δr_{syst} (%)	$\delta r_{\text{tot}}^{\text{exp}}$ (%)
30 – 34	1.85	0.4	11.7	11.7
34 – 39	1.99	0.5	10.0	10.0
39 – 44	2.15	0.7	8.6	8.7
44 – 50	2.37	0.9	7.6	7.7
50 – 60	2.70	1.0	6.7	6.8
60 – 70	3.14	1.6	5.8	6.1
70 – 80	3.66	2.5	5.0	5.5
80 – 90	4.28	3.6	4.5	5.8
90 – 110	4.97	4.0	4.2	5.8
110 – 130	7.00	7.5	3.9	8.4
130 – 150	9.01	12.6	3.6	13.1

TABLE VII: Ratios of the differential cross sections in the $|y^{\text{jet}}| < 0.8, y^\gamma \cdot y^{\text{jet}} < 0$ rapidity region to the $1.5 < |y^{\text{jet}}| < 2.5, y^\gamma \cdot y^{\text{jet}} > 0$ rapidity region.

p_T^γ bin (GeV)	Ratio (r)	δr_{stat} (%)	δr_{syst} (%)	$\delta r_{\text{tot}}^{\text{exp}}$ (%)
30 – 34	1.51	0.4	11.9	11.9
34 – 39	1.62	0.5	10.6	10.6
39 – 44	1.74	0.7	9.1	9.1
44 – 50	1.90	0.9	8.0	8.0
50 – 60	2.16	1.0	7.0	7.0
60 – 70	2.53	1.7	5.9	6.2
70 – 80	2.92	2.5	5.0	5.6
80 – 90	3.44	3.7	4.5	5.8
90 – 110	4.14	4.1	4.3	5.9
110 – 130	5.73	7.6	4.0	8.6
130 – 150	7.27	12.8	3.7	13.3

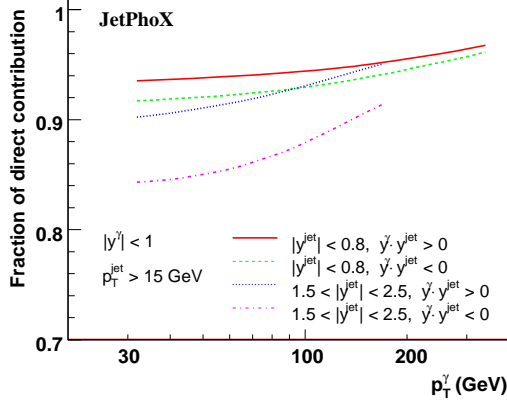


FIG. 9: The ratios of the $p\bar{p} \rightarrow \gamma + \text{jet} + X$ cross section with just the direct (non-fragmentation) contribution to the total (direct+fragmentation) cross section estimated with JETPHOX for each measured region.

TABLE VIII: Ratios of the differential cross sections in the $1.5 < |y^{\text{jet}}| < 2.5$, $y^\gamma \cdot y^{\text{jet}} < 0$ rapidity region to the $1.5 < |y^{\text{jet}}| < 2.5$, $y^\gamma \cdot y^{\text{jet}} > 0$ rapidity region.

p_T^γ bin (GeV)	Ratio (r)	δr_{stat} (%)	δr_{syst} (%)	$\delta r_{\text{tot}}^{\text{exp}}$ (%)
30 – 34	0.49	0.5	10.9	10.9
34 – 39	0.50	0.6	9.7	9.7
39 – 44	0.49	0.9	8.0	8.0
44 – 50	0.49	1.1	6.7	6.8
50 – 60	0.52	1.3	5.6	5.8
60 – 70	0.53	2.2	5.0	5.4
70 – 80	0.54	3.4	4.8	5.8
80 – 90	0.59	4.9	4.8	6.8
90 – 110	0.54	5.8	4.7	7.4
110 – 130	0.64	10.8	4.5	11.7
130 – 150	0.63	18.4	4.3	18.9
150 – 200	0.97	32.5	4.1	32.8

the data presented in this Letter, show a need for an improved and consistent theoretical description of the γ +jet production process.

We are very thankful to P. Aurenche, M. Fontannaz, J. P. Guillet, and M. Werlen for providing the JETPHOX package, useful discussions and assistance with theoretical calculations. We thank the staffs at Fermilab and collaborating institutions, and acknowledge support from the DOE and NSF (USA); CEA and CNRS/IN2P3 (France); FASI, Rosatom and RFBR (Russia); CAPES, CNPq, FAPERJ, FAPESP and FUNDUNESP (Brazil); DAE and DST (India); Colciencias (Colombia); CONACyT (Mexico); KRF and KOSEF (Korea); CONICET and UBACyT (Argentina); FOM (The Netherlands); Science and Technology Facilities Council (United Kingdom); MSMT and GACR (Czech Republic); CRC Program, CFI, NSERC and WestGrid Project (Canada); BMBF and DFG (Germany); SFI (Ireland); The Swedish

TABLE IX: Ratios of the differential cross sections in the $|y^{\text{jet}}| < 0.8$, $y^\gamma \cdot y^{\text{jet}} > 0$ rapidity region to the $1.5 < |y^{\text{jet}}| < 2.5$, $y^\gamma \cdot y^{\text{jet}} < 0$ rapidity region.

p_T^γ bin (GeV)	Ratio (r)	δr_{stat} (%)	δr_{syst} (%)	$\delta r_{\text{tot}}^{\text{exp}}$ (%)
30 – 34	3.81	0.4	10.4	10.4
34 – 39	4.00	0.5	8.8	8.8
39 – 44	4.39	0.8	6.9	6.9
44 – 50	4.82	1.0	5.5	5.6
50 – 60	5.23	1.2	4.6	4.7
60 – 70	5.97	1.9	4.3	4.7
70 – 80	6.81	2.8	4.5	5.3
80 – 90	7.20	4.1	4.6	6.1
90 – 110	9.21	4.8	4.6	6.7
110 – 130	10.91	8.7	4.6	9.9
130 – 150	14.31	14.8	4.4	15.4
150 – 200	38.29	23.9	4.2	24.2

TABLE X: Ratios of the differential cross sections in the $|y^{\text{jet}}| < 0.8$, $y^\gamma \cdot y^{\text{jet}} < 0$ rapidity region to the $1.5 < |y^{\text{jet}}| < 2.5$, $y^\gamma \cdot y^{\text{jet}} < 0$ rapidity region.

p_T^γ bin (GeV)	Ratio (r)	δr_{stat} (%)	δr_{syst} (%)	$\delta r_{\text{tot}}^{\text{exp}}$ (%)
30 – 34	3.10	0.4	10.7	10.7
34 – 39	3.25	0.5	9.5	9.5
39 – 44	3.55	0.8	7.4	7.5
44 – 50	3.86	1.0	6.0	6.1
50 – 60	4.18	1.2	4.9	5.0
60 – 70	4.81	1.9	4.5	4.9
70 – 80	5.43	2.9	4.5	5.4
80 – 90	5.80	4.1	4.6	6.2
90 – 110	7.67	4.9	4.7	6.8
110 – 130	8.93	8.8	4.7	10.0
130 – 150	11.55	14.9	4.5	15.5
150 – 200	35.48	23.9	4.3	24.3

Research Council (Sweden); CAS and CNSF (China); Alexander von Humboldt Foundation; and the Marie Curie Program.

- [a] Visitor from Augustana College, Sioux Falls, SD, USA.
- [b] Visitor from The University of Liverpool, Liverpool, UK.
- [c] Visitor from ICN-UNAM, Mexico City, Mexico.
- [d] Visitor from II. Physikalisches Institut, Georg-August-University, Göttingen, Germany.
- [e] Visitor from Helsinki Institute of Physics, Helsinki, Finland.
- [f] Visitor from Universität Zürich, Zürich, Switzerland.
- [‡] Deceased.

- [1] P. Aurenche, J. Lindfors, Nucl. Phys. **B168**, 296 (1980); P. Aurenche et al., Phys. Lett. B **140**, 87 (1984); Zeit.

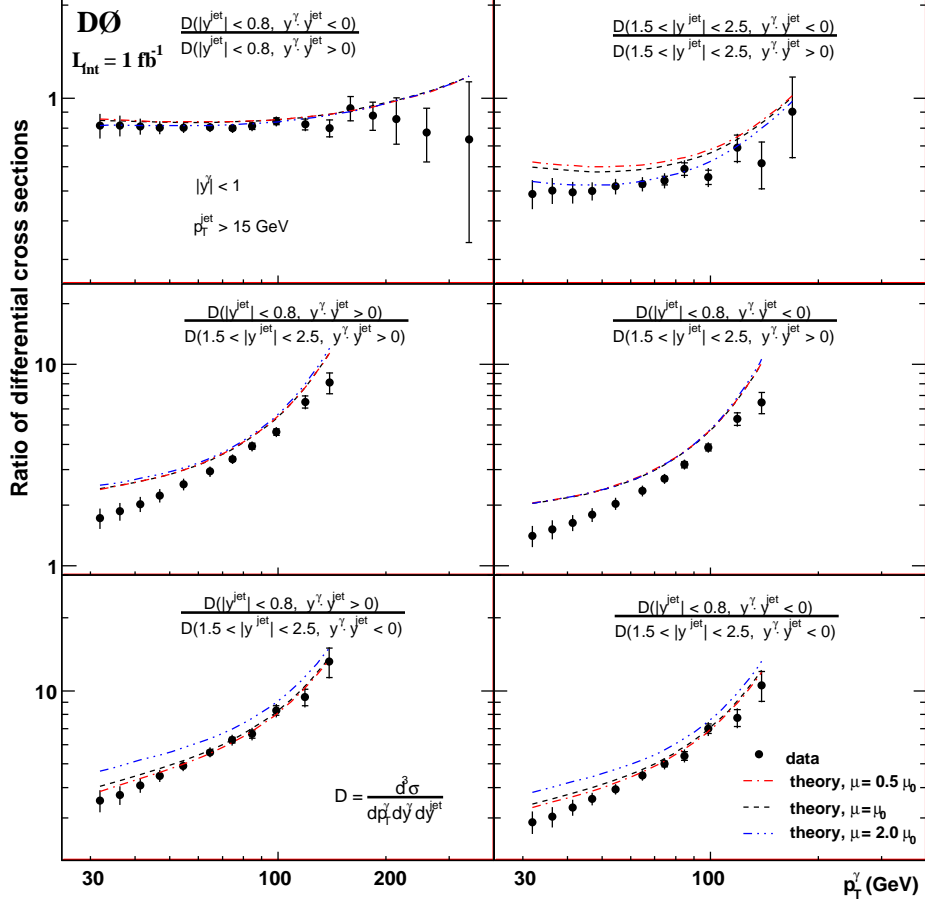


FIG. 10: The ratios between the differential cross sections in each y^{jet} region. The solid vertical error bars correspond to the statistical and systematic uncertainties added in quadrature while the horizontal marks indicate the statistical uncertainty. NLO QCD theoretical predictions for the ratios, estimated using JETPHOX, are shown for three different scales: $\mu_{R,F,f} = \mu_0$, $0.5\mu_0$, and $2\mu_0$, where $\mu_0 = p_T^* f(y^*)$.

- Phys. C **29**, 423 (1985).
- [2] J. F. Owens, Rev. Mod. Phys. **59**, 465 (1987).
- [3] A. P. Contogouris, N. Mebarki, E. N. Argyres, and S. D. P. Vlassopoulos, Phys. Rev. D **35**, 1584 (1987).
- [4] P. Aurenche et al., Phys. Rev. D **39**, 3275 (1989).
- [5] W. Vogelsang and A. Vogt, Nucl. Phys. **B453**, 334 (1995).
- [6] A. D. Martin et al., Eur. Phys. J. C **4**, 463 (1998).
- [7] J. Alitti et al. (UA2 Collaboration), Phys. Lett. B **263**, 544 (1991).
- [8] D. Acosta et al. (CDF Collaboration), Phys. Rev. D **65**, 112003 (2002).
- [9] B. Abbott et al. (D0 Collaboration), Phys. Rev. Lett. **84**, 2786 (2000); V. M. Abazov et al. (D0 Collaboration), Phys. Rev. Lett. **87**, 2518 (2001).
- [10] V. M. Abazov et al. (D0 Collaboration), Phys. Lett. B **639**, 151 (2006); B **658**, 285 (2007).
- [11] $y = 1/2 \ln(E - p_L)/(E + p_L)$, where E is the energy and p_L is the longitudinal momenta with respect to the z axis.
- [12] F. Abe et al. (CDF Collaboration), Phys. Rev. D **57**, 67 (1998).
- [13] T. Akesson et al. (ISR-AFS Collaboration), Zeit. Phys. C **34**, 293 (1987).
- [14] J. Alitti et al. (UA2 Collaboration), Phys. Lett. B **299**, 174 (1993).
- [15] A. Aktas et al. (H1 Collaboration), Eur. Phys. J. C **38**, 437 (2005).
- [16] F.D. Aaron et al. (H1 Collaboration), arXiv:0711.4578 [hep-ex] (2007).
- [17] S. Chekanov et al. (ZEUS Collaboration), Phys. Lett. B **595**, 86 (2004).
- [18] S. Chekanov et al. (ZEUS Collaboration), Eur. Phys. J. C **49**, 511 (2007).
- [19] T. Sjöstrand et al., Comput. Phys. Commun. **135**, 238 (2001), we use PYTHIA v6.3.
- [20] W. K. Tung et al., JHEP **0702**, 053 (2007).
- [21] W. K. Tung, arXiv:hep-ph/0409145 (2004).
- [22] T. Andeen et al., FERMILAB-TM-2365 (2007).
- [23] V. M. Abazov et al. (D0 Collaboration), Nucl. Instrum. Meth. Phys. Res. A **565**, 463 (2006).
- [24] Pseudorapidity is defined as $\eta = -\ln[\tan(\theta/2)]$, where θ is the polar angle with respect to the proton beam direction.
- [25] V. M. Abazov et al. (D0 Collaboration), Phys. Rev. Lett. **95**, 051802 (2005); Phys. Rev. D **76**, 012003 (2007).
- [26] D. Bandurin and N. Skachkov, Phys. Part. Nucl. **35**, 66

- (2004).
- [27] C. Peterson, T. Rognvaldsson, and L. Lönnblad, *Comput. Phys. Commun.* **81**, 15 (1994).
- [28] R. Brun and F. Carminati, CERN Program Library Long Writeup **W5013**, (1993), unpublished.
- [29] G. C. Blazey et al., arXiv:hep-ex/0005012 (2000).
- [30] R. J. Barlow and C. Beeston, *Comput. Phys. Commun.* **77**, 219 (1993).
- [31] Only statistical uncertainties in the γ +jet MC, dijet MC and data samples are taken into account in the calculation of χ^2 .
- [32] The uncertainty ranges are quoted for a low p_T^γ first and for a high p_T^γ second.
- [33] B. Abbott et al. (D0 Collaboration), *Phys. Rev. D* **64**, 032003 (2001).
- [34] G. D. Lafferty and T. R. Wyatt, *Nucl. Instrum. Meth. Phys. Res. A* **355**, 541 (1995).
- [35] P. Aurenche et al., *Nucl. Phys.* **B297**, 661 (1988); F. Aversa et al., *Nucl. Phys.* **B327**, 105 (1989).
- [36] S. Catani et al., *JHEP* **05**, 028 (2002).
- [37] L. Bourhis, M. Fontannaz, and J. P. Guillet, *Eur. Phys. J. C* **2**, 529 (1998).
- [38] This scale choice is suggested by M. Fontannaz and J. P. Guillet. Private communication.
- [39] A. D. Martin, R. G. Roberts, W. J. Stirling, and R. S. Thorne, *Phys. Lett. B* **604**, 61 (2004).
- [40] S. Alekhin, *Phys. Rev. D* **68**, 014002 (2003).
- [41] S. Chekanov et al. (ZEUS Collaboration), *Eur. Phys. J. C* **42**, 1 (2005).
- [42] E. L. Berger and J.-W. Qiu, *Phys. Lett. B* **248**, 371 (1990).
- [43] P. Aurenche et al., *Phys. Rev. D* **73**, 094007 (2006).
- [44] G. Sterman and W. Vogelsang, *JHEP* **0102**, 016 (2001).